aerospace

MDPI

Article

Aerodynamic Shape Optimization of Wing–Fuselage Intersection for Minimum Interference Drag

Nuno M. B. Matos [1,2,*] and André C. Marta [2]

[1] Research and Development, Tekever UAS, 2500-750 Caldas da Rainha, Portugal
[2] IDMEC, Instituto Superior Técnico, Universidade de Lisboa, 1049-001 Lisboa, Portugal; andre.marta@tecnico.ulisboa.pt
* Correspondence: nuno.matos@tecnico.ulisboa.pt

Abstract: Interference drag in wing–fuselage intersection regions is a complex aerodynamic phenomenon where secondary flows and separation conditions might occur if not properly addressed in the aircraft design. In this work, the optimal shape of the intersection region between the wing and fuselage of a MALE UAV is studied using gradient-based optimization and free-form deformation techniques. High-fidelity fluid computational dynamics solving the RANS equations are employed, together with the corresponding adjoint formulation to compute the gradients of the aerodynamic metrics. Different shape deformation techniques are explored for both the fuselage and wing, and several combinations of design variables are studied. Fuselage shape deformations were found to be more efficient in the removal of the secondary flow near the wing root trailing edge. Reducing the cross-sectional area of the fuselage near the wing leading edge and increasing it near the trailing edge was shown to reduce drag, demonstrating that secondary flow mitigation is more relevant than reduced frontal area. A 2% total drag reduction was obtained by simultaneously shaping both the fuselage and the wing in the intersection region. The optimized wing–fuselage interface remained sharp, without fairings, due to the limitation of the deformation technique to modify the original topology.

Keywords: secondary flow; fuselage shaping; free-form deformation; high-fidelity CFD; gradient-based optimization; adjoint method

Academic Editor: Bosko Rasuo

Received: 17 March 2025
Revised: 12 April 2025
Accepted: 23 April 2025
Published: 24 April 2025

Citation: Matos, N.M.B.; Marta, A.C. Aerodynamic Shape Optimization of Wing–Fuselage Intersection for Minimum Interference Drag. *Aerospace* **2025**, *12*, 369. https://doi.org/10.3390/aerospace12050369

1. Introduction

Interference drag is one of the most complex aspects of the aerodynamic performance of an aircraft. It is usually driven by complex secondary flows that arise at the physical junction of between components subjected to a given flow [1]. These can be the connection between tail and fuselage, landing gear and fuselage, or, the most classical, between wing and fuselage.

Although extensively studied in other fields, such as axial rotors [2,3], the study of aerodynamic interference drag between typical aircraft parts is still relatively lacking. Relevant work has been performed especially in engine mount drag assessment [4–6], and new concept wings such as high-aspect-ratio braced-wing designs [7,8]. Experimental studies have been conducted on the integration of wing and fuselage [9–11], where the presence of the secondary flows was demonstrated and the benefits of using some shape conforming interface was found beneficial to reduce induced drag. This problem has already been tackled with numerical methods, with some high-fidelity Computational Fluid Dynamics (CFD) models able to accurately capture the secondary flows [12,13]. With the increase in computational power and the progress on efficient optimization

algorithms, some optimization studies have recently tried to address the intersection of aircraft surfaces [14–16]. Despite these progresses, the deep understanding of the wing–fuselage phenomena necessary to drive design optimality is yet to be achieved. This might be due to not only the complex secondary flows found but also the complexity of the shape deformation optimization limitations, as addressed next.

The understanding of the effects of a wing and fuselage intersection requires knowledge of the complex 3D aerodynamics, which is only possible to acquire accurately either with wind tunnel testing [9–11] or computational simulations [12,13,17,18]. If the aerodynamic interference is overlooked, the wing–fuselage connection can induce separation in the root sections of the wing earlier than expected and/or generate excessive interference drag [12,13,17]. Although low- to mid-fidelity analyses can be performed, such as 3D panel methods, to evaluate the overall aerodynamics of a complete configuration aircraft, these do not predict 3D aerodynamic viscous effects, such as boundary layer phenomena [19,20]. Thus, the use of high-fidelity analysis tools, such as Reynolds-averaged Navier–Stokes (RANS) with turbulence models, is of the utmost importance to accurately predict the influence of the intersection between components.

Regarding the complexity of the shape deformation, the question posed that and needs to be addressed is, what is the best way to define the intersection between two components? There are certain case-specific guidelines to follow: usage of blended, integrated fairings; extension of the root section near the fuselage instead of using a blunt edge; and reduction in the cross-flow influence of the fuselage [9]. However, recent tools that support the usage of efficient gradient-based optimization techniques can now be used to not only assess these claims but also search, within optimality conditions, the best geometries to better design wing–fuselage junctions [14–16]. One such tool is the MACH-Aero framework [21], which allows the usage of adjoint-based optimization techniques [22] with high-fidelity CFD solvers, such as ADFlow [23,24], an open-source developed aerodynamic RANS solver software.

There are many shape deformation methods applicable to 3D objects, such as [25] basis vector, domain element, partial differential equation, discrete, polynomial and spline, CAD based, analytical, and free-form deformation (FFD).

A straightforward and simple approach is to have the geometry defined by a given set of parameters whose changes allow for the manipulation of the 3D shape. This is useful for conceptual or preliminary design studies that depend on generative designs [25,26] or require low computational cost. However, the resulting deformation dependency on the problem itself requires costly finite differences or time consuming analytical sensitivities for gradient-based optimization.

In contrast, the FFD method is independent of the body being deformed, allowing for a wider range of applications and suitable for adjoint-based gradient optimization, where the differentiated methods can be formulated without the knowledge of the shape being deformed [27,28]. FFD has been used in structural optimization [29,30] and is particularly effective in aerodynamic optimization using high-fidelity CFD [26] due to its capability of transforming not only surface shapes but also volume meshes accordingly, thus reducing the need of costly re-meshing. However, it is more difficult to accurately translate the resulting FFD shape into a set of enfineering parameters for a proper component definition. It usually implies the use of the final geometry as-is or the reconstruction of the deformation from the original geometry with a decoder algorithm to determine the parameter set that reproduces such final geometry in the most accurate possible way. Radial Basis Function (RBF)-based morphing techniques have been proposed to address shape deformation [31]. Although compatible with CAD tools [16], this method is neither accurately linked to

typical shape parametrization variables of aircraft surfaces nor allows for individually shape deformation approaches on intersecting geometries.

Given the larger design space that FFD allows, which translates into a wider range of shapes, it was the shape deformation method elected for this work. In terms of fuselage and wing surface shape deformation, the FFD techniques incorporated into the MACH-Aero framework [21] were used and adapted, allowing for flexibility in shape deformation techniques, as well as the individual deformation of each component. The FFD shape deformation can also be coupled with structural deformations to allow internal structure shape deformations for aerostructural coupling [30].

In this work, a methodology for wing and fuselage shape deformation is presented, along with wing–fuselage intersection shape optimization, to better understand and capture the optimal design features of a wing–fuselage intersection in subsonic dominated flows to minimize the drag increase due to these interference effects. The proposed methodology is demonstrated in a test case based on a fixed-wing, medium-altitude long-endurance (MALE) UAV, under development at Tekever UAS. The main contributions of this work are (1) the exploration of optimal wing–fuselage intersection shapes; (2) the identification of existing gaps and difficulties in optimizing intersecting aerodynamic aircraft components; (3) the exploration of design variable impact on optimal shape; and (4) finding the limitations within similar shape deformation methods.

2. Shape Deformation Methods

Different shape deformation techniques were used for both wing and fuselage to account for specific design features over the intersection region. These are described next.

2.1. Fuselage Manipulation Strategies

The fuselage shape was controlled by manipulating the FFD control points defining a selected fitted volume box around the fuselage. Examples of FFD boxes are shown in Figure 1, where different refinement levels are used.

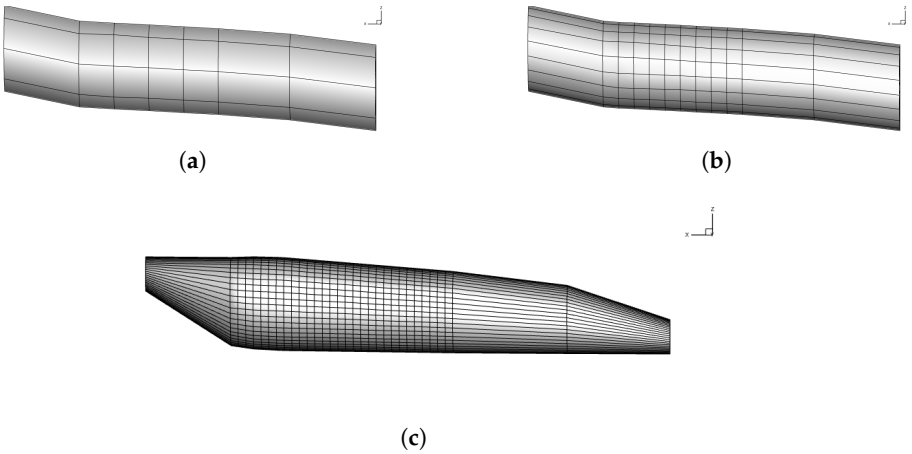

(**a**) (**b**)

(**c**)

Figure 1. Fuselage FFD boxes with varying refinement levels (number of control points in the wing–fuselage intersection zone of interest). (**a**) Coarsest mesh 5×5 (not used). (**b**) Medium mesh 10×10 (used in strategy (1)). (**c**) Finest mesh 30×30 (used in strategy (2)).

Instead of using all FFD box nodes as control points of the fuselage shape, only a selected few were selected to restrict the the fuselage deformation to its surface near the wing intersection. The active control points are delimited between a front fuselage cross-section some length ahead of the wing root leading edge (LE) and a rear section some

length after the wing root trailing edge (TE). The coordinates of the remaining (inactive) control points are kept frozen during the optimization.

This approach was studied in two different strategies regarding the FFD control point freedom: (1) using radial displacements relative to its longitudinal axis (case *r*) and (2) using normal distribution-based deformations (case *n*).

For the first strategy (1), the radial displacement of each active point is controlled by a design variable. Thus, the number of design variables corresponds to the active FFD nodes in the defined wing–fuselage intersecting region of interest, leading to a relatively large number of variables in the optimization. While, intuitively, finer box meshes would allow better manipulation of local fuselage shapes, it was verified that using a reduced number of FFD nodes led to smoother fuselage surface during the optimization process, preventing negative volumes in volume mesh morphing and allowing for larger deformations in each optimization iteration. Thus, the medium refinement FFD box was used, as shown in Figure 1b. An example of this shape deformation strategy can be seen in Figure 2b.

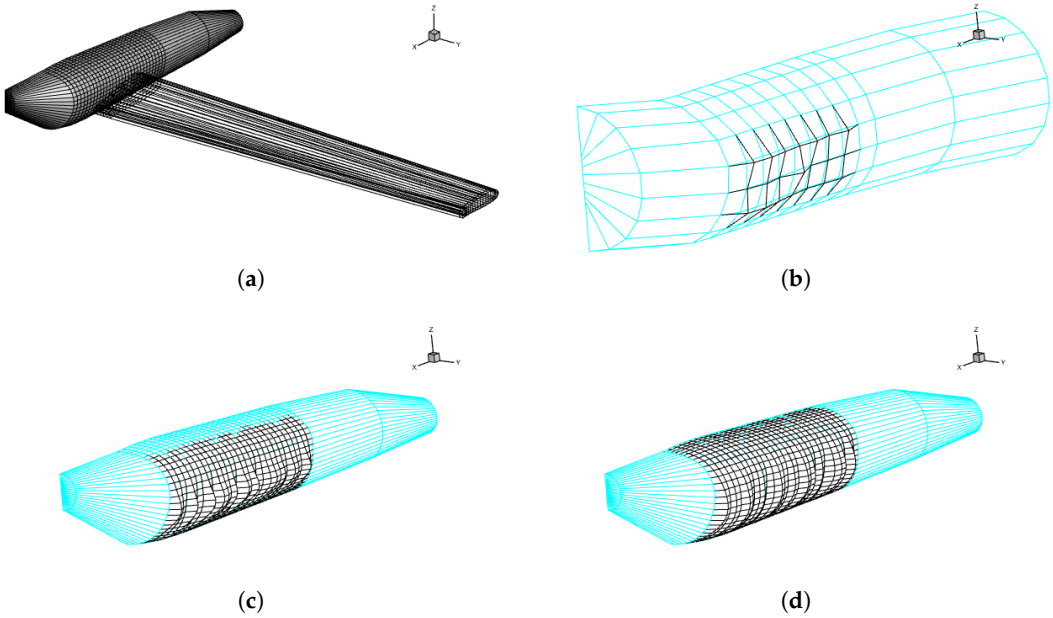

Figure 2. Fuselage FFD boxes (blue) with the deformation strategies previewed (black). (**a**) Original most refined fuselage FFD box with refinement in the intersection region. (**b**) Radial displacement deformation. (**c**) Sectional normal distribution function radial deformation with low σ. (**d**) Sectional normal distribution function radial deformation with high σ.

For the second strategy (2), the deformation of the set of active points that belong to a given FFD box cross-section are controlled by a single parametric function, thus considerably reducing the total number of design variables compared to strategy (1). A simplified normal distribution-based deformation description was implemented, which only uses three parameters. The radial coordinate variation of a given control point i is obtained as

$$\Delta r_i = e^{-0.5\frac{(r_i-\mu)^2}{\sigma^2}} k_{scale}\,, \tag{1}$$

where the parameters μ, σ and k_{scale} represent the mean value, which adjusts the location of the maximum variation; the standard deviation, which controls the spreading of the variation around the control point; and a scaling factor, which determines the magnitude of the variation, respectively. A demonstration of such deformation in a single fuselage FFD box cross-section is illustrated in Figure 3 for generic parameters.

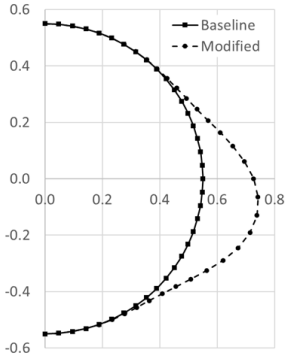

Figure 3. Normal distribution-based shape deformation of a given fuselage cross-section.

Using this strategy, different fuselage shape outlines can be obtained through the control of only n design variables, with n being the number of active FFD box cross-sections corresponding to the scaling factor k_{scale}. Examples of possible deformations can be seen in Figure 2c,d, where random parameters were used. The impact of the design parameter σ can be observed from these examples: low values have a less smooth approach but better local deformations (Figure 2c), while high values tend to smooth the fuselage shape with the setback of diminishing local changes (Figure 2d).

2.2. Wing Manipulation Strategies

Similar to the fuselage, the wing can be manipulated through the usage of the FFD points in a structured manner. In order to reduce the design space, only three main strategies were considered for the wing shape deformation: (1) root section scaling in both longitudinal chord x-direction (case s_x) and vertical thickness z-direction (case s_z); (2) wing horizontal and vertical position relative to fuselage (cases h and v, respectively); and (3) twist angle near the intersection region (case t). The scaling was opted for instead of a free deformation to retain similar airfoil properties. This set of design variables allows the wing to position itself differently on the fuselage surface, as well as to deform its root section during the optimization procedure of the wing–fuselage intersection.

For both scaling and twist, a single-design-variable quadratic deformation function is used, ranging from a maximum in the first refined FFD spanwise section, given by the design variable value, to the original baseline (undeformed) value in the last refined FFD spanwise section. This ensures that the wing remains unaltered from the last spanwise refinement point of the FFD box until the wing tip, minimizing the wing shape deformation and keeping the focus on its fuselage intersection region.

For the scaling, the scaling factor for a given spanwise point ($span_i$) in the intersecting region is

$$s_i = 1 + x_s \left(\frac{span_f - span_i}{span_f - span_0} \right)^2, \tag{2}$$

where x_s is the scaling design variable, and $span_0$ and $span_f$ are the first and last refined FFD zone spanwise location, respectively. Similarly, the twist deformation at a given spanwise position is calculated as

$$t_i = x_t \left(\frac{span_f - span_i}{span_f - span_0} \right)^2, \tag{3}$$

where, x_t represents the twist design variable. This allows a continuous wing deformation near the fuselage intersection region while avoiding unnecessary meshing transformation problems and reducing the number of design variables.

Examples of possible wing deformations can be seen in Figure 4 for the different strategies, where the undeformed wing FFD box is also included for reference. Notice the refinement of the FFD box in the zone corresponding to the interface between the fuselage ($span_0$) and the wing ($span_f$), where the local deformations (scaling (1) and twist (3)) are applied.

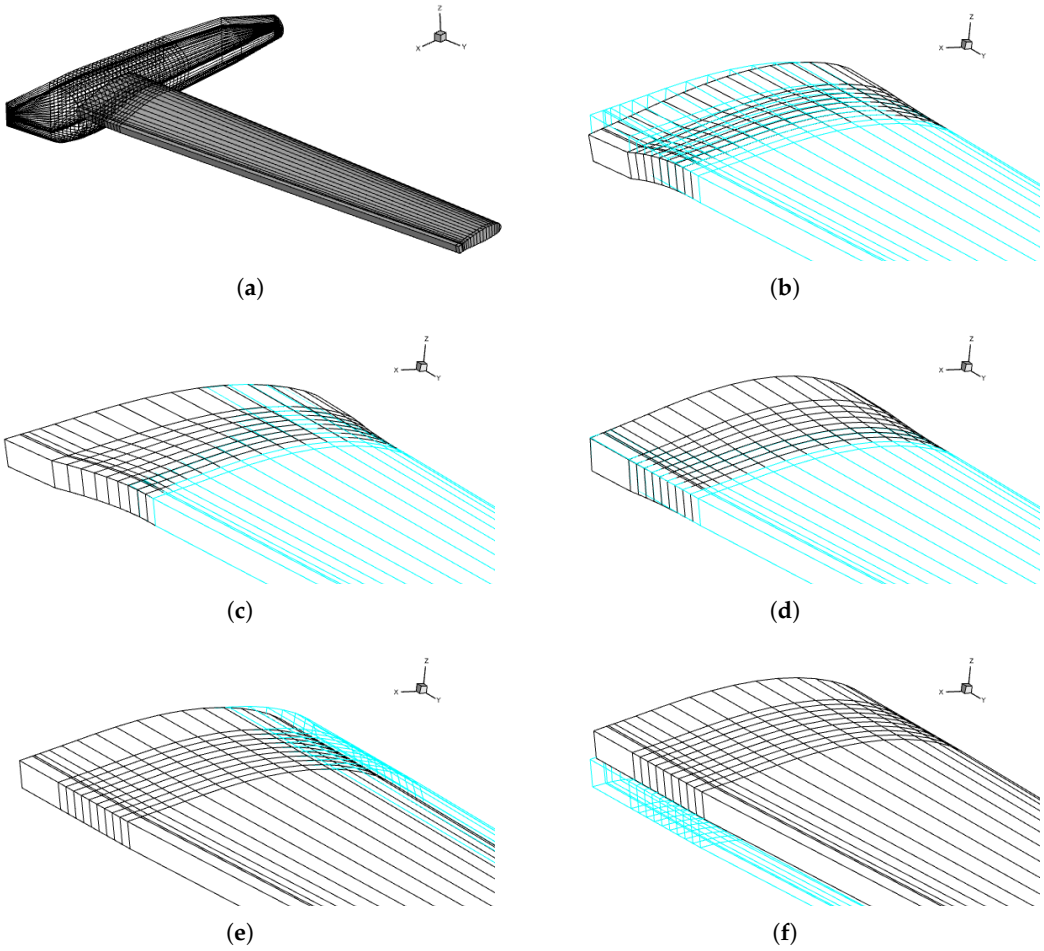

Figure 4. Wing FFD box (blue) with deformation strategies previewed (black). (**a**) Undeformed wing FFD box with refinement at intersection region. (**b**) Local twist deformation. (**c**) Local chord scaling. (**d**) Local thickness scaling. (**e**) Horizontal relative position. (**f**) Vertical relative position.

2.3. Summary

The optimization cases presented in this work are composed of a combination of the different fuselage and wing deformation strategies discussed previously, as summarized in Table 1, where their corresponding naming, number of associated design variables, and lower and upper bounds are listed.

The design variable bounds were chosen based on three aspects: (i) real-case application deformation; (ii) intersecting region meshing deformation stability; and (iii) overall meshing deformation stability. Nonetheless, their values are believed to be sufficient for the overall goal of this work—to evaluate challenges in wing–fuselage intersection optimization and to discuss wing–fuselage reduced interference designs.

The applied deformation methods allow for the individual control of each component [14]. The intersecting region is handled by, first, calculating the moved intersection points and, then, re-shaping both fuselage and wing points with an interpolation made between both deformed components.

Table 1. Shape deformation strategies, naming, associated number of design variables and bounds.

Strategy	Description	# DVs	Lower Bound	Upper Bound
r	Fuselage radial point deformation	21 *	−0.1	0.1
n	Fuselage normal function deformation	28 **	−0.1	0.1
t	Wing twist deformation	1	−5.0	5.0
s_x	Wing chord scaling deformation	1	0.0	0.1
s_z	Wing thickness scaling deformation	1	0.0	1.0
h	Wing horizontal position deformation	1	−0.1	0.1
v	Wing vertical position deformation	1	−0.1	0.1

* Number of active FFD points based on the coarsest FFD box (7 longitudinal points times 3 vertical points).
** Number of active longitudinal refined FFD cross-section sections on the finest FFD box.

The naming of the optimization cases in Sections 4 and 4.4 results from the juxtaposition of the strategies names of the particular combination used.

3. Aerodynamic Baseline Analysis

Before addressing shape optimization, the aerodynamic characterization of the baseline test case is performed to identify the wing–fuselage interference phenomenon. In this work, the intersection between the wing and the fuselage of the Tekever ARX, a 12 m span MALE UAV under development by Tekever UAS, is studied. The current UAV detailed design, as well as the simplified geometry used in this work, are shown in Figure 5.

(**a**)

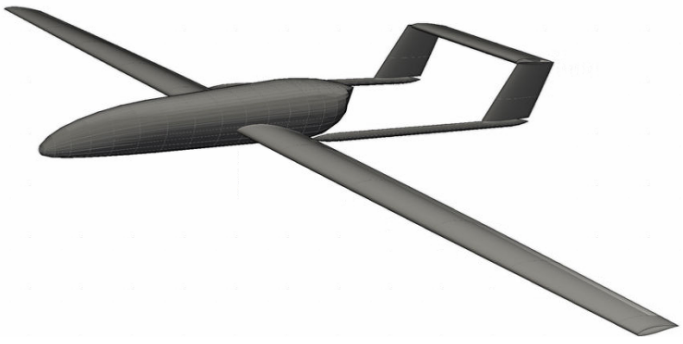

(**b**)

Figure 5. Test case UAV: Tekever ARX. (**a**) Current detailed design. (**b**) Simplified geometry for analysis.

The simplified geometry has a cleaner fuselage and, more importantly, a blunt connection between wing and fuselage which was engineered on purpose to ultimately verify the final result of the optimization process. The booms and tail are presented for comparison purposes, but these elements were not considered in the optimization. As for the operating conditions used, standard leveled flight conditions at the expected flight speeds for each

angle of attack operating point were used, assuming an altitude of $1000 ft$. These calculations are performed using as basis the lift coefficient C_L curve and assuming the maximum takeoff mass configuration of 600 kg using the lift calculation formula for trim flight as

$$V = \sqrt{\frac{W}{\frac{1}{2}\rho S_{ref} C_L}} \quad , \tag{4}$$

where W, ρ, and S_{ref} are the weight, air density, and reference area of the aircraft.

The CFD software used was ADFlow (version 2.12) [23,24], which solves the RANS equations. The Spalart–Almaras turbulence model was selected since it had been differentiated for the adjoint-based gradient evaluation, which was subsequently used in the shape optimization studies.

As for the geometry, the custom developed *TekAero* package was used, where geometric generators based on parametric functions create, as closely as possible, the current aircraft design. Features include the generation of the wing based on general shape parameters (sweep, chord, twist, and dihedral) and the generation of the fuselage based on the adaptation of an imported *stl* mesh.

3.1. Mesh Convergence Study

Each CFD mesh was generated using the overset technique with four initial structured meshes: wing mesh, fuselage mesh, collar mesh at the wing–fuselage intersection region, and background mesh. Both fuselage and wing meshes overlap each other, requiring the definition of their intersection through the usage of the collar mesh. The latter was generated through *TekAero*, where geometric intersection is carried out and automatic collar grid generation is conducted with both body and surface fitting. Figure 6 illustrates both the coarsest R_0 and finest R_4 mesh used in this study, where only the right half of the aircraft was modeled due to symmetry.

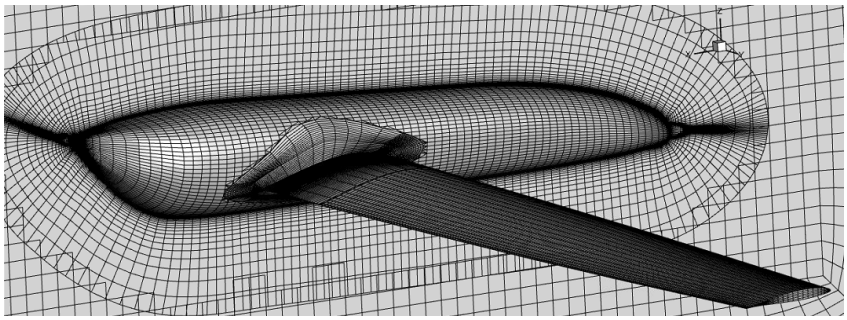

(**a**)

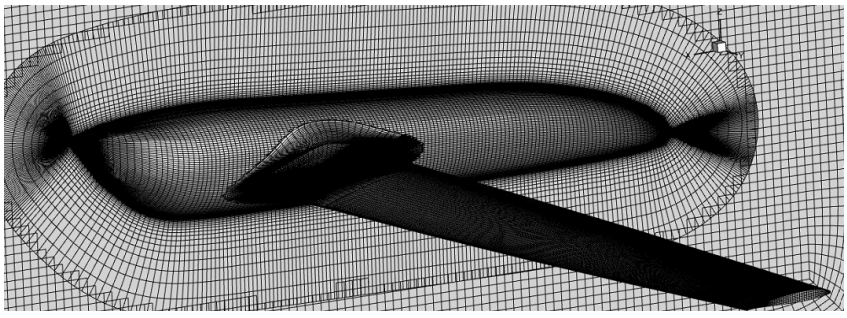

(**b**)

Figure 6. Grid refinement levels. (**a**) Coarsest R_0 mesh. (**b**) Finest R_4 mesh.

A total of five CFD mesh refinement levels were tested, with the UAV operating a zero angle of attack (AoA), producing the lift coefficient C_L and drag coefficient C_D (in

drag counts) shown in Figure 7, where the separate pressure C_{Dp} and viscous C_{Dv} drag contributions are also included.

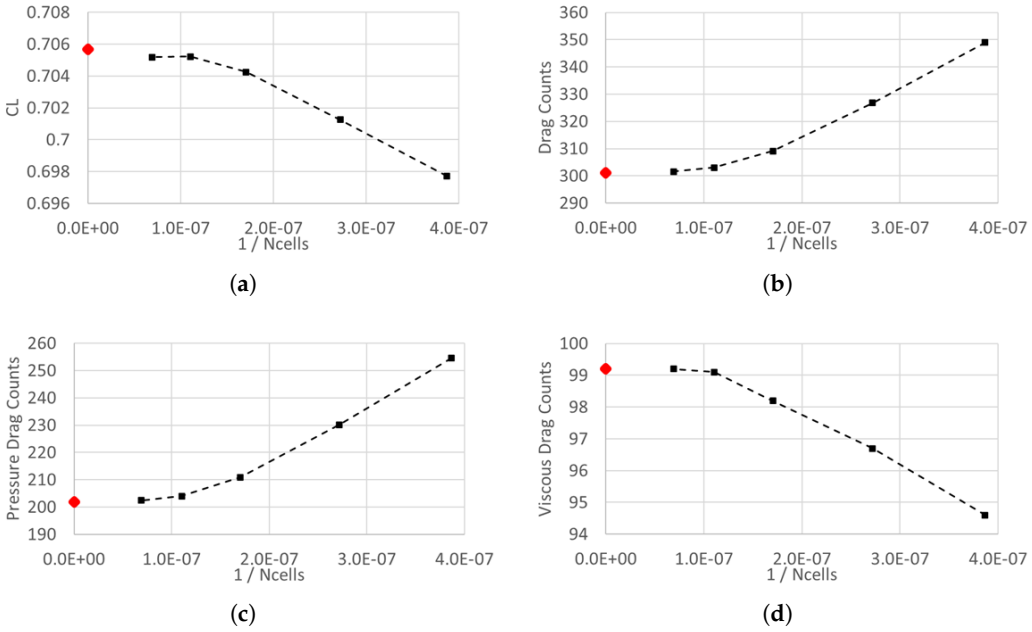

Figure 7. Grid convergence study and Richardson extrapolation. (**a**) Lift coefficient C_L. (**b**) Drag coefficient C_D. (**c**) Pressure drag coefficient C_{Dp}. (**d**) Viscous drag coefficient C_{Dv}.

Each of the four plots of the grid refinement study exhibits an expected convergence to a value R_E shown in red, which was estimated using the Richardson extrapolation [32,33]. These extrapolated values R_E were used as reference to assess the solution relative error for each grid level, with the results summarized in Table 2. The last column displays the computational (CPU) cost normalized using the finest grid level as reference.

Table 2. Solution error estimate and computational cost by grid level.

Mesh	Value				Relative Error				CPU Cost
	C_L	C_{D_v}	C_{D_p}	C_D	C_L	C_{D_v}	C_{D_p}	C_D	
R_0	0.6977	0.0095	0.0255	0.0349	1.13%	4.65%	−26.04%	−15.91%	0.02
R_1	0.7013	0.0097	0.0230	0.0327	0.63%	2.53%	−14.01%	−8.54%	0.03
R_2	0.7043	0.0098	0.0211	0.0309	0.20%	1.02%	−4.45%	−2.66%	0.11
R_3	0.7052	0.0099	0.0204	0.0303	0.07%	0.11%	−1.03%	−0.66%	0.41
R_4	0.7052	0.0099	0.0202	0.0302	0.07%	0.01%	−0.24%	−0.17%	1.00
R_E	0.7057	0.0099	0.0202	0.0301	-	-	-	-	

As expected, the lift coefficient converges considerably faster than the drag coefficient, as the latter depends greatly on the near-wall mesh refinement. Interestingly, the main source of error on the drag coefficient results from the pressure drag calculation, for which the fuselage was found to contribute the most. In contrast, even with the coarsest mesh (R_0), the viscous drag coefficient presents an error below 5%. Having in mind that the optimization iteration process implies the recurrent run of the flow and adjoint solver, with the latter having similar computational cost to the former, the medium refinement level mesh R_2 was chosen for this work, as it exhibits the best trade-off between accuracy, with estimated relative error below 5% for all quantities analyzed, and computational cost.

3.2. Wing–Fuselage Interference

The baseline UAV configuration was characterized, with particular focus on the wing–fuselage interference, running ADFlow for an AoA ranging from −4° to 12°, to map

different operating conditions. The baseline configuration exhibits typical lift and drag curves, as seen in Figure 8a, where stall effects appear at around 6° of angle of attack with the slope reduction in C_L and increase in C_D. Since this particular wing design has an incidence angle of around 4°, this point corresponds to an effective wing AoA of around 10°. The maximum endurance ratio $C_L^{1.5}/C_D$ is obtained at 4° and the maximum range ratio C_L/C_D occurs for an AoA of around 2°, as seen in Figure 8b.

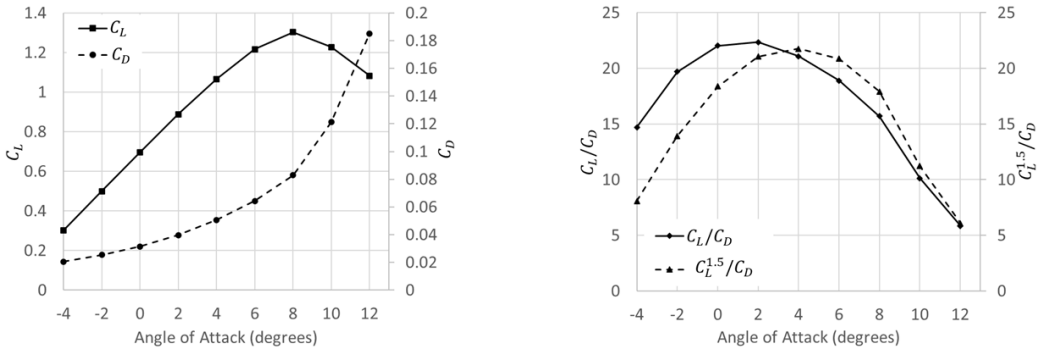

(**a**) (**b**)

Figure 8. Baseline configuration aerodynamic metrics as function of angle of attack. (**a**) Lift and drag coefficients. (**b**) Range $\left(\frac{C_L}{C_D}\right)$ and endurance $\left(\frac{C_L^{1.5}}{C_D}\right)$ metrics.

The development of stall with increasing AoA is mostly due to the growing separation occurring on the wing suction side (upper surface), but the secondary flows around the wing and fuselage intersection also play a role, as attested by Figure 9, where the surface skin friction sign in the longitudinal direction is displayed. The zero value represents the separation lines and negative values (in red) represent regions of reversed flow.

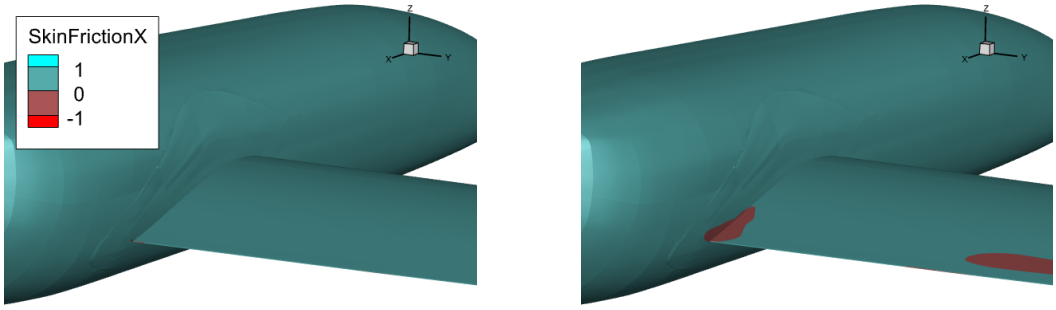

(**a**) (**b**)

Figure 9. Skin friction sign on longitudinal direction (negative regions indicate reverse flow). (**a**) Operating at $\alpha = 0°$. (**b**) Operating at $\alpha = 6°$.

The flow separation phenomenon appearing on the wing and fuselage intersection starts at the trailing edge and progressively grows towards the leading edge with increased AoA, indicating the increase in secondary flow intensity, as attested by the visualization of the streamlines in that region shown in Figure 10. Notice that, for an AoA of 2° or 4°, there is no significant wing stall, but a separation bubble appears and starts growing.

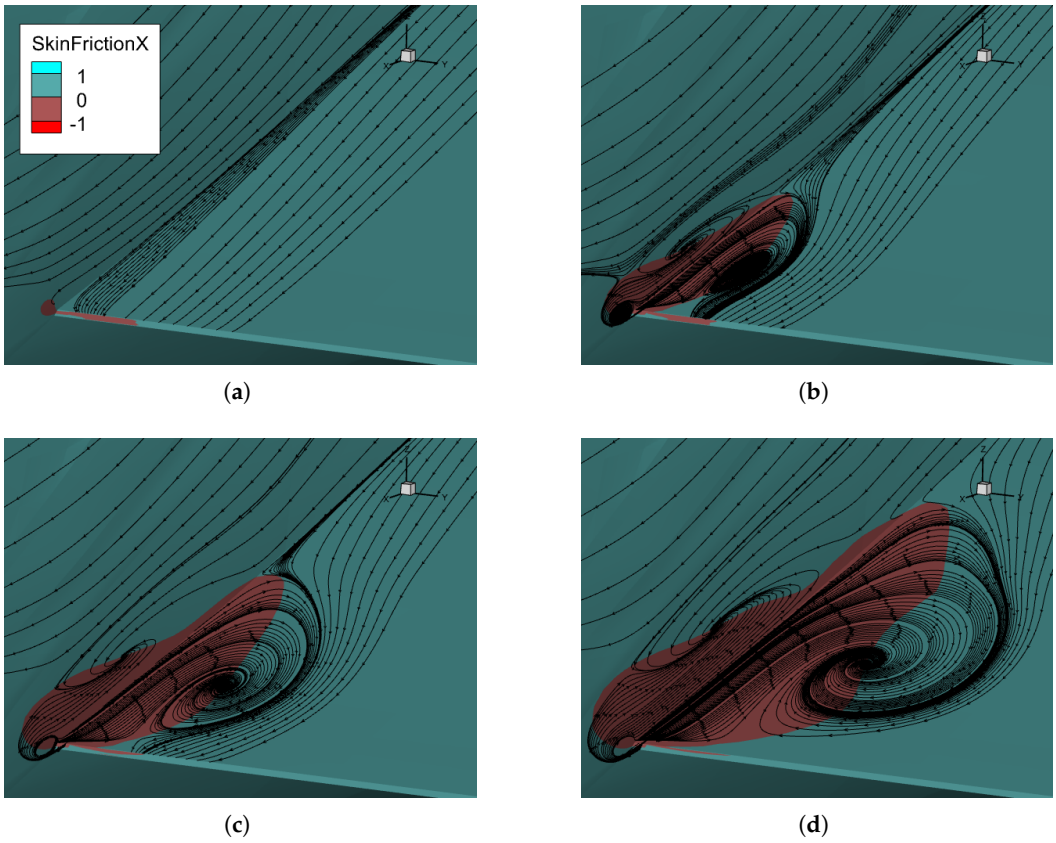

(**a**) (**b**)

(**c**) (**d**)

Figure 10. Skin friction sign on the longitudinal direction with overlaid streamlines: detail of secondary flow intensity growth with AoA. (**a**) Operating at $\alpha = 0°$. (**b**) Operating at $\alpha = 2°$. (**c**) Operating at $\alpha = 4°$. (**d**) Operating at $\alpha = 6°$.

These results demonstrate that not only the mesh refinement level and the aerodynamic numerical model used are capable of capturing such complex, localized flow interactions. More importantly, they clearly show the negative interaction between the fuselage and the wing in terms of aerodynamic interference. The ultimate goal of this work is to mitigate this negative interaction effect by performing shape optimization at the connection region, as addressed in the next sections.

4. Aerodynamic Shape Optimization

The optimization approach was performed by first studying the individual fuselage and wing deformation methodologies and then combining both. For a clearer understanding of the overall optimization process, the results will presented in a sequential fashion, from the simplest cases to the more complex, with intermediate remarks, discussion, identification of gaps and problems found throughout.

The first UAV optimization studies dealt with single operating points, corresponding to an AoA of 6° condition, at which significant interference occurs, as documented in Section 3.2. The objective function to be minimized is the drag coefficient C_D, which is a metric of the intensity of the secondary flow at the wing–fuselage interface. The optimization problem was then posed in standard form as

$$\begin{aligned} \underset{\boldsymbol{x}}{\text{minimize}} \quad & C_D(\boldsymbol{x}) \\ \text{subject to} \quad & \Delta C_L(\alpha, \boldsymbol{x}) = 0 \end{aligned}, \tag{5}$$

where $\boldsymbol{x}$ is the vector of all design variables (DVs) used in each case, and $\Delta C_L(\alpha)$ is the variation of lift coefficient for each operating point α relative to the baseline (Figure 8a. The lift coefficient constraint is only applied to the final study cases to assess its impact on the optimal shape. Although relevant for complete aircraft, the pitching moment constraint was not considered in the optimization mainly due to the following: (1) the small impact on the overall pitching moment due to the localized shape deformation approach and (2) the lacking of the full aircraft configuration, namely the horizontal stabilizer.

The optimization problem is solved using the gradient-based SLSQP algorithm, which has been shown to perform well in aerodynamic shape optimization problems [34]. This algorithm is part of the `pyoptsparse` package [22], and it was used with a convergence tolerance of 10^{-6} and with a maximum of 500 iterations. The gradient information is computed using the efficient adjoint formulation within the MACH-Aero framework [24].

As mentioned in Section 2.3, the optimization cases are named by combining the naming of all cases used. For example, if an optimization case used both *r* and *t* deformation strategies, its naming would be *rt* or *tr*.

4.1. Fuselage Optimization

For the fuselage-only optimization, both radial (case *r*) and normal distribution function (case *n*) shape deformation strategies were analyzed individually. The parameters of the normal distribution function (Equation (1)) were set to $\sigma = 0.15$ and $\mu = 0.2$, which placed the maximum deformation coincident with the wing location while softening the local deformation, and were kept constant throughout the remaining work.

Both optimization cases produced identical drag reduction, as summarized in Table 3, after a similar number of iterations (counted through the number of gradient evaluations), but case *n* required a higher number of function calls. That higher number of function calls was a consequence of a less than ideal DV scaling, which had a detrimental impact in the step size during the line search, with the optimizer having been observed taking larger steps than desired in the initial iterations, implying additional function calls for the roll-back step.

Table 3. Fuselage single-operating-point optimization: drag reduction.

Case	Function Calls	Gradient Calls	ΔC_D
n	33	19	−1.29%
r	18	18	−1.29%

For both cases, the optimal solutions were limited by many DVs reaching their bounds, as seen in Figure 11, where each bar corresponds to the value of each design variable ordered along the longitudinal axis from leading to trailing edge. From the DV ordering, it can already be concluded that both solutions exhibit the same shape deformation pattern to reduce drag: the fuselage cross-section is decreased near the wing LE region and increased near the wing TE region. Although not intuitive, the benefit of increasing the cross-sectional radius at the TE region to reduce the wing–fuselage interference drag outweighs the drag penalty of increasing the frontal area. While better results could have been achieved with wider DV bounds, these imposed values corresponding to a relatively change of ±10% of the original fuselage radius were deemed reasonable to not significantly impact the UAV internal payload area. As a side benefit, those relatively strict bounds contributed to the successful mesh morphing during the optimization iterations.

The fuselage optimal shape deformation near the wing intersection that minimized the interference drag can be observed in Figure 12, where the contour of the longitudinal surface skin friction sign is overlaid, along with figure insets for the top and rear views. From a geometry perspective, a very similar deformation can be clearly seen for both

optimizations—a shrank fuselage near the wing LE and an expanded fuselage near the wing TE. Comparing both geometries in more detail, case *r* provided a smoother solution, which was expected due to its lower number of DVs that cause each one to affect a larger number of FFD surface points.

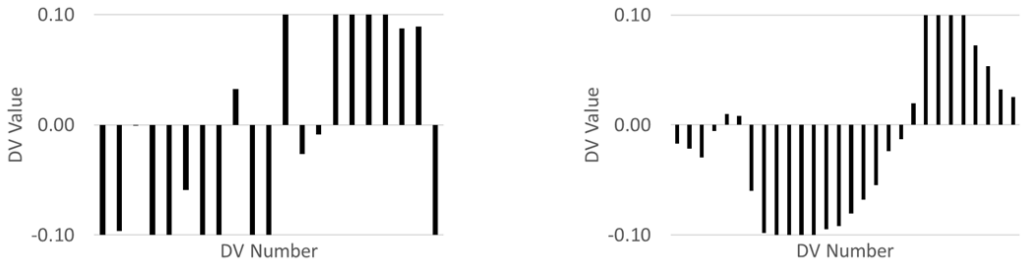

(**a**) (**b**)

Figure 11. Fuselage single-operating-point optimization: design variables (ordered longitudinally from front to rear). (**a**) Case *r*. (**b**) Case *n*.

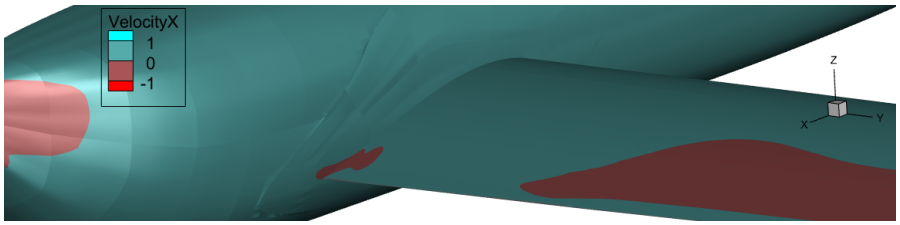

(**a**)

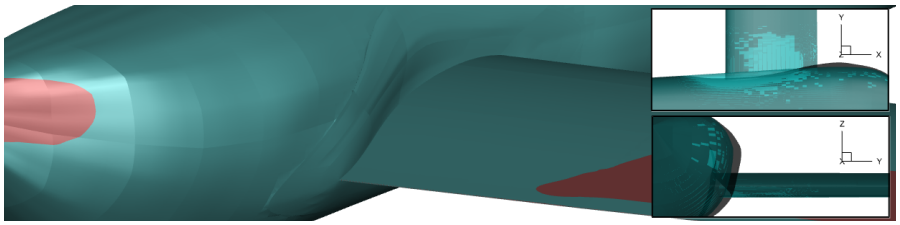

(**b**)

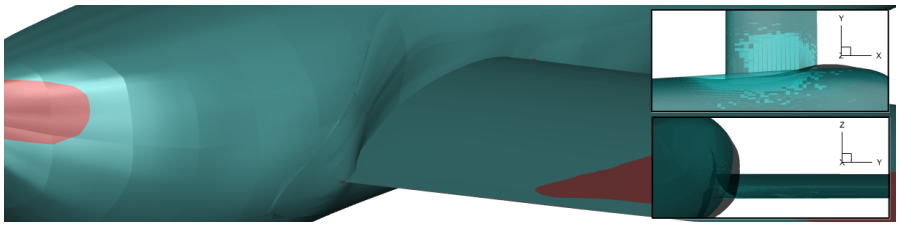

(**c**)

Figure 12. Fuselage single-operating-point optimization: optimal shape deformation. (**a**) Baseline (for reference). (**b**) Case *r*. (**c**) Case *n*.

The skin friction sign plots indicate that the original separation flow region induced by the wing–fuselage intersection has been completely removed with the optimized fuselage shapes. The expansion of the fuselage TE wing region surface increases the local flow velocity, thus energizing it and making it more resistant to the local adverse pressure gradient.

4.2. Wing Optimization

For the wing-only optimization, the complexity of the problem was increased incrementally. First, case *t* was used to study the intersecting twist effect; then, case *ts* with

combined twist and airfoil scaling was studied; and finally, case *tshv* added the effect of the wing position.

Table 4 summarizes the drag reduction obtained for these three cases. Compared to the fuselage-only results, all wing-only cases led to much smaller drag reductions. In fact, case *ts* was not successful, probably due poor scaling of the airfoil parameters. Clearly, the most significant contribution comes from the wing vertical (v) and longitudinal (h) position DVs. The number of iterations (same as gradient calls) is low in all cases analyzed as a result of the relatively low impact of these DVs on the overall drag reduction.

Table 4. Wing single-operating-point optimization: drag reduction.

Case	Function Calls	Gradient Calls	ΔC_D
t	13	2	−0.02%
ts	12	1	-
tshv	5	5	−0.43%

The initial shape shown in Figure 12a can be compared to the optimized wing shape near the fuselage connection for the different wing-only deformation strategies shown in Figure 13, where the inset figures contain the top and back view and compare the baseline shape (blue) to the optimized (black). In contrast to the fuselage-only optimization results seen in Figure 12, none of the skin friction contour plots show any clear reduction in the separation bubble in the connection region. In fact, both cases *t* and *tshv* produced a slight increase. Thus, the drag reduction obtained is a consequence of either (i) a better placement of the wing within the fuselage cross-section or (ii) a better overall pressure distribution obtained through the usage of twist in the wing–fuselage intersection region.

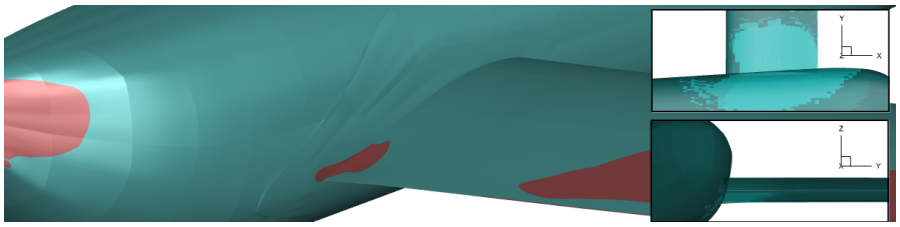

(**a**)

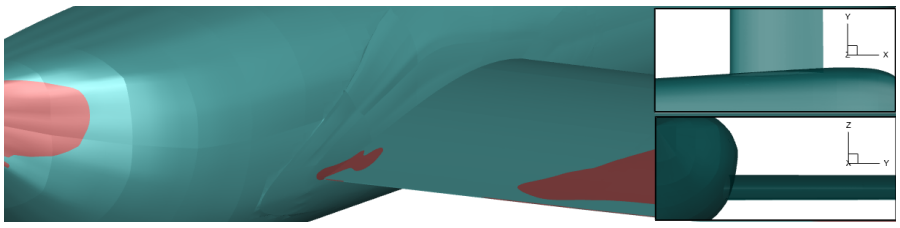

(**b**)

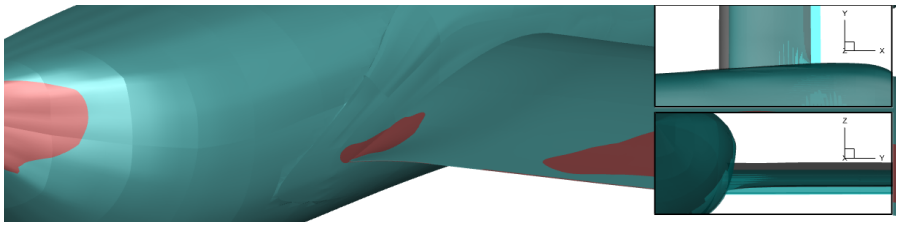

(**c**)

Figure 13. Wing single-operating-point optimization: optimal shape deformation. (**a**) Case *t*. (**b**) Case *ts*. (**c**) Case *tshv*.

Even though the findings might be specific to the particular UAV studied, it was found that reduced interference drag could be obtained by modifying the wing with (a) increasing twist near the intersection region; (b) moving vertically, upward to the mid-fuselage position; (c) moving longitudinally forward; and (d) no airfoil scaling on both longitudinal and vertical directions.

4.3. Combined Fuselage and Wing Optimization

By combining fuselage and wing shape deformation design variables, the optimization produced a larger reduction in total drag when compared to the reductions obtained through the usage of fuselage-only or wing-only deformation, as attested in Table 5. This is unsurprising since the optimizer could take advantage of more DVs, creating a larger design space to explore. Furthermore, using radial fuselage deformations (strategy *r*) along with the wing shape deformation variables (strategies *t*, *s*, *h* and *v*) produced the highest drag reduction shape for the unconstrained problem. However, the opposite was observed when the lift constraint condition was added.

Table 5. Combined fuselage and wing single-operating-point optimization: drag reduction.

Case	Function Calls	Gradient Calls	ΔC_D
tshvr	36	22	−1.85%
tshvn	38	23	−1.75%
tshvr with C_L constraint	15	14	−1.34%
tshvn with C_L constraint	53	33	−1.42%

The differences between cases are mostly due to the local normal distribution function shapes having a fixed maximum location (set with parameter μ) that does not cease to coincide with the wing when the latter changes position with the optimization cycles, so minimal changes in the wing position occurred for these cases.

When the lift constraint is added to the optimization problem, the decrease in drag is not as large. However, slight improvements were still experienced when compared to the unconstrained fuselage-only or wing-only deformation strategies, highlighting the importance of using combined deformation strategies when approaching this problem.

Noticeably, the number of both function and gradient calls change depending on whether the lift coefficient constraint is used, increasing for the *tshvn* case and decreasing for the *tshvr* case. This can be due to a different number of factors, such as reduction in feasible design space, local minima changes, or constraint function violation.

The visualization of the combined fuselage and wing optimal shape can be seen in Figure 14, where the contour plots and inset figures follow the same formatting as before. Compared to the initial shape shown in Figure 12a, the secondary flow that leads to separation at the intersection region between wing and fuselage completely disappears with the shape optimization in all cases, except in the *tshvn* unconstrained case where a minimal separation bubble still persisted. Interestingly, the constraint lift coefficient cases present smoother overall surface deformations while achieving similar results, suggesting that the inclusion of the lift constraints can enhance feasible surfaces for manufacturing scenarios. This is particularly seen in the constrained *tshvn* case, where the optimal shape is similar to the one found by the constrained *tshvr* case.

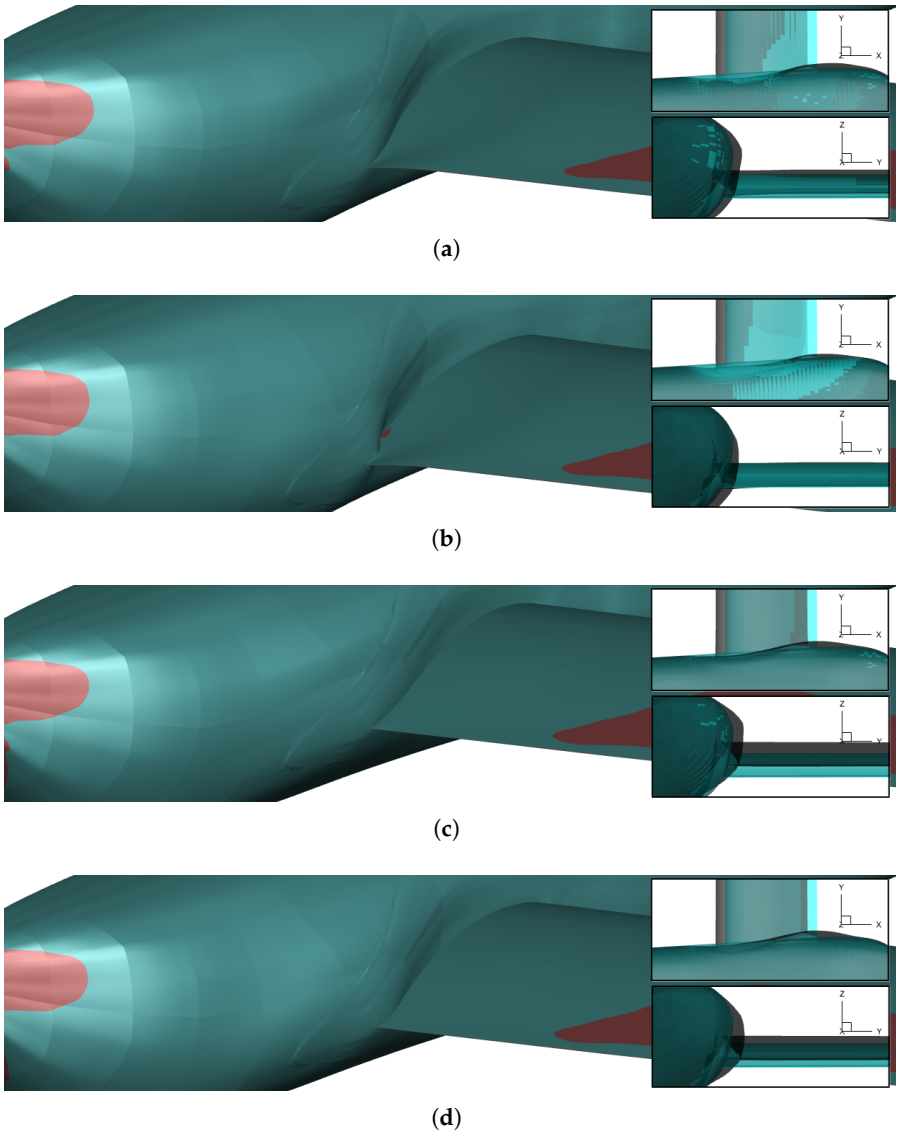

Figure 14. Combined fuselage and wing single-operating-point optimization: optimal shape deformation. (**a**) Case *tshvr*. (**b**) Case *tshvn*. (**c**) Case *tshvr* with lift coefficient constraint. (**d**) Case *tshvn* with lift coefficient constraint.

4.4. Multi-Operating-Point Optimization

As seen from the previous results, the optimizations produced very tailored shapes that performed very well for the considered 6° AoA operating condition. However, single operating points often lack the understanding of the off-design performance [7,35], with it being usual for those optimal solutions to perform poorly at other operating points, sometimes even worse than the baseline design. For this reason, a multi-operating-point optimization approach was considered, in which a second operating point, corresponding to the zero AoA condition, was added to the optimization problem. The zero AoA condition was chosen for being representative of the UAV cruise design condition. At the cruise condition, there is almost no secondary flow-induced separation for the baseline shape, as seen in Figure 10a, and it is desired that the shape optimization preserves this characteristic. The optimization problem statement was reformulated to

$$\underset{x}{\text{minimize}} \quad \frac{\sum C_{D_i}(\boldsymbol{x})}{n} \quad , \tag{6}$$

where the subscript i refers to the operating condition and n is the number of operating conditions. Notice that no lift coefficient constraint was added in the multi-point optimization case, mainly due to (i) the unlikely capability of the optimizer to maintain the lift coefficient for both operating points and (ii) the expected minimal changes in lift coefficient during the optimization.

The multi-operating-point shape optimization problem was solved using the same set of DVs that produced the best solution in the single-operating-point optimization; that is, the combined fuselage and wing optimization case *tshvr* was selected. The optimizer found a shape that reduced the total drag by -1.46% and -1.81% for null and 6° of AoA, respectively. Recalling from Table 5 that the single-operating-point *tshvr* case produced a -1.85% drag reduction at 6° of AoA, it can be concluded that the multi-operating-point approach produced a better overall solution, both on- and off-design, with a minimal impact on the critical high AoA condition performance. These results were obtained with a difference in lift coefficient of -2.53% for the null AoA case and -0.83% at the positive AoA operating point. Additionally, the changes in pitching moment accumulated to less then 2%.

The resulting optimal shape can be seen in Figure 15, which is similar to the shape found for the single-operating-point case optimization (Figure 14a), with a reduction in cross-sectional area at the leading edge region and an increase near the trailing edge. Interestingly, the surfaces obtained are smoother than unconstrained single-operating-point optimizations. Again, the interference effect was mitigated and the flow separation eliminated at 6° AoA in the wing–fuselage trailing region.

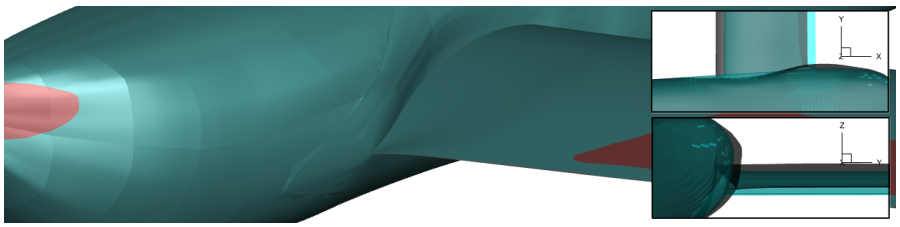

Figure 15. Combined fuselage and wing multi-operating-point optimization: optimal shape deformation for case *tshvr*, contours at $\alpha = 6^\circ$.

The comparison of the UAV complete fuselage and wing between the baseline design and the one with optimally shaped wing–fuselage interface for the multi-operating-point *tsvhr* case can be observed in Figure 16. The contour of the pressure coefficient reveals that both distributions remain very similar, since the shape optimization was exclusively located at the wing–fuselage intersection region. But, as expected, there are some significant local differences, which were driven by those local fuselage and wing shape deformations. On the wing root upper surface, the pressure suction peak is less intense and occurs closer to the LE, making the pressure recovery more gradual and thus with a milder adverse pressure gradient, which corroborates the observation of the elimination of flow separation in that region. Also, the wing has moved upward and forward, which caused a change in the fuselage pressure towards the rear and, more significantly, on its side. This, compounded with the cross-section area variation along the fuselage near the wing position, resulted in a significant fuselage pressure increase near the wing LE and decrease near the wing TE regions.

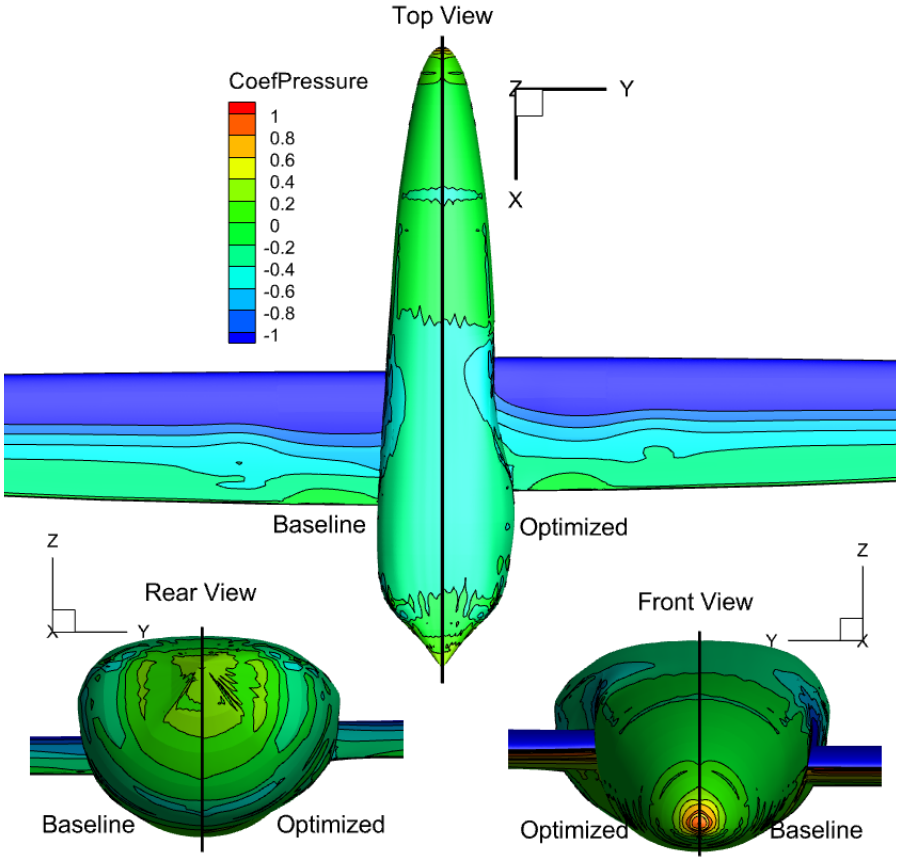

Figure 16. Combined fuselage and wing multi-operating-point optimization: comparison of pressure coefficient between baseline and optimal shape.

5. Wing–Fuselage Intersection Design Guidelines

Throughout this work, several wing–fuselage intersection shape optimization cases were analyzed using different shape deformation strategies. This section intends to summarize the main findings in terms of choosing the shape deformation that leads to the most efficient designs with the least costly process.

The fuselage shape optimization has shown that the design variables chosen had a high impact on the secondary flow phenomenon, being able to completely remove flow separation at the region near the wing root TE upper surface, reducing the total drag, as demonstrated in in Section 4.1. Furthermore, increasing the fuselage cross-sectional area around the wing TE was found to be beneficial to the overall drag reduction, as the reverse flow phenomenon has a high impact on the total drag when compared to pressure drag induced by a larger exposure of surface to the flow. On the other hand, reducing the cross-sectional area near the wing LE, up to around mid-point in the chordwise direction, helped reduce the total drag.

The wing shape deformation focused on the reduction in the overall drag not by reducing the secondary flow separation phenomenon on the upper surface but by finding an overall better pressure distribution. This was corroborated by the lack of reverse flow area reduction seen in all single-operating-point wing optimization cases in Section 4.2. For the specific test case UAV design, the wing-related shape DVs had minimal impact on mitigating the secondary flow phenomenon, which might have been in part due the fact they were restricted to simple transformation functions with just a few DVs related to wing position and root airfoil scaling. Certainly, adding the airfoil shape to the DVs set could alter this, but that is not common practice for the intersection region design. Significant

improvement was found by repositioning the wing on the fuselage, as attested with case *tshv* analyzed, which led to the maximum drag reduction, only limited by the DV bounds to avoid computational meshing deformation instabilities. The optimization showed that the wing should be preferentially placed mid-height at the fuselage's widest location and moved forward further away from the sharp ending of the fuselage.

Unsurprisingly, the combination of both fuselage and wing optimization produced the best designs, as demonstrated in Sections 4.3 and 4.4. Recalling constrained case *tsvhr*, in order to better interpret the optimal shape design found, Figure 17 exhibits the changes in longitudinal velocity and pressure coefficient from the baseline to the optimal shape, where red and blue represent negative and positive variations, respectively. The variations in these quantities are clear around the wing–fuselage intersection region, where the shape deformation took place. Looking carefully at Figure 17a, the fuselage cross-sectional area reduction near the wing LE and increase toward the TE cause an initial airflow speed reduction and then acceleration, making the flow more energized and thus less prone to separation. This behavior is consistent with the pressure coefficient variation observed in Figure 17b: the increase in surface pressure in the fuselage region in front of the wing LE and the reduction in the fuselage near the wing TE produce a pressure gradient along the wing root chord that is less adverse and that no longer leads to secondary flow separation

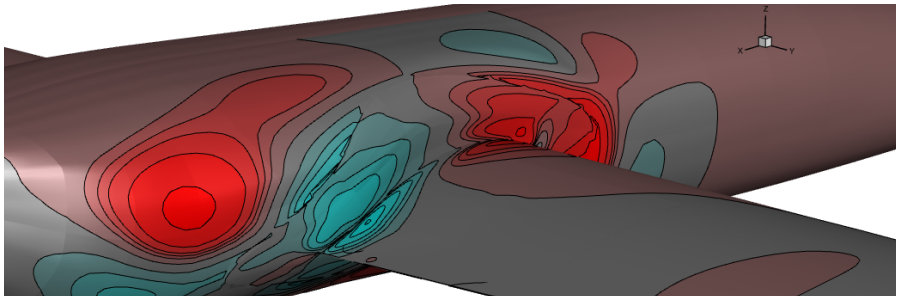

(**a**)

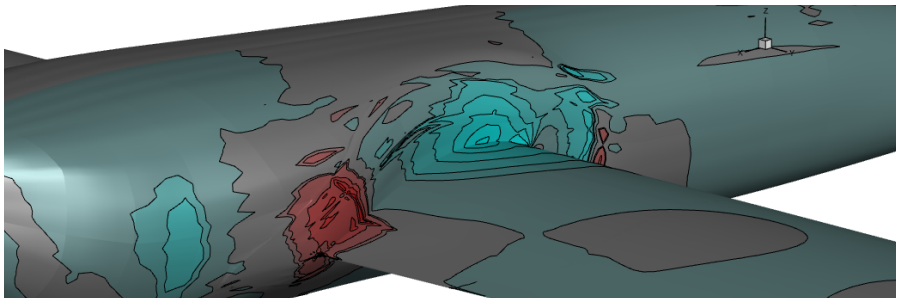

(**b**)

Figure 17. Combined fuselage and wing single-operating-point optimization: variation from baseline to optimal shape (red and blue represent negative and positive variations, respectively). (**a**) Near surface longitudinal velocity variation. (**b**) Surface pressure coefficient variation.

As a final remark, notice that the optimal shape found did not produce any fairing, with the connection between the wing and the fuselage still being sharp with close to 90° intersection angles. Two hypotheses can justify the blunt wing–fuselage connection found: (1) the sharp shape is actually optimal; (2) the optimal shape was limited by the deformation strategies used. The latter hypothesis is more likely correct, highlighting a gap in interference aerodynamic drag reduction with FFD shape manipulation—a baseline (initial) sharp wing–fuselage connection is maintained by the optimization procedure due to limitations within the shape deformation algorithm.

6. Conclusions

The minimum-drag optimal wing–fuselage intersection shape of a UAV was studied. It was found that typical wing shape deformations focused on overall drag reduction while fuselage shape deformations focused on mitigating the secondary flow separation. While the best designs resulted from the simultaneous deformation of both the fuselage and wing at the connection region, the biggest contribution to total drag reduction came from the fuselage shape deformation variables included. A reduction in aerodynamic total drag of almost 2% was found to be possible by addressing just the connection region between the wing and the fuselage while maintaining similar lift performance, which confirmed the importance of reducing interference effects in multi-surface aircraft configurations.

An important gap was found in optimizing an initially sharp wing–fuselage connection configuration that is believed to exist for every similar shape optimization scenario—topological characteristics from the initial configuration remain on the final optimized shape design. To address this gap, the shape deformation algorithms must be improved to be capable of smoothing interface edges and automatically creating fairing surfaces.

Author Contributions: Conceptualization, N.M.B.M. and A.C.M.; methodology, N.M.B.M. and A.C.M.; software, N.M.B.M.; validation, N.M.B.M. and A.C.M.; formal analysis, N.M.B.M. and A.C.M.; investigation, N.M.B.M.; resources, N.M.B.M. and A.C.M.; data curation, N.M.B.M. and A.C.M.; writing—original draft preparation, N.M.B.M.; writing—review and editing, N.M.B.M. and A.C.M.; visualization, N.M.B.M.; supervision, A.C.M.; project administration, A.C.M.; funding acquisition, A.C.M. All authors have read and agreed to the published version of the manuscript.

Funding: The authors acknowledge Fundação para a Ciência e a Tecnologia (FCT) for its financial support via the project LAETA Base Funding (DOI: 10.54499/UIDB/50022/2020).

Data Availability Statement: The data presented in this study are available on request from the corresponding author.

Acknowledgments: The authors would like to thank Tekever UAS for supporting the production of this article by offering all the needed data to successfully produce the analyses here shown.

Conflicts of Interest: Author Nuno M. B. Matos was employed by the company Tekever UAS. The remaining authors declare that the research was conducted in the absence of any commercial or financial relationships that could be construed as a potential conflict of interest.

Abbreviations

The following abbreviations are used in this manuscript:

AoA	Angle of Attack
CFD	Computational Fluid Dynamics
DV	Design Variable
FFD	Free-Form Deformation
LE	Leading Edge
MALE	Medium-Altitude Long-Endurance
RANS	Reynolds-Averaged Navier–Stokes
SLSQP	Sequential Least Squares Programming
TE	Trailing Edge
UAV	Unmanned Aerial Vehicle

References

1. Langston, L.S. Secondary Flows in Axial Turbines—A Review. *Ann. N. Y. Acad. Sci.* **2001**, *934*, 11–26. [CrossRef] [PubMed]
2. Babu, S.; Anish, S. Aerodynamic performance of profiled endwalls with upstream slot purge flow in a linear turbine cascade having pressure side separation. *Phys. Fluids* **2021**, *33*, 015119. [CrossRef]

3. Zhang, B.; Zhu, H.; Yao, C.; Liu, C.; Zhang, Z. Investigation on film cooling and aerodynamic performance of blade tip with tangential jet cooling scheme at transonic flow. *Aerosp. Sci. Technol.* **2021**, *118*, 107067. [CrossRef]
4. Brodersen, O. Drag Prediction of Engine-Airframe Interference Effects Using Unstructured Navier-Stokes Calculations. *J. Aircr.* **2002**, *39*, 927–935. [CrossRef]
5. Stankowski, T.P.; MacManus, D.G.; Sheaf, C.T.; Grech, N. Aerodynamic Interference for Aero-Engine Installations. In Proceedings of the 54th AIAA Aerospace Sciences Meeting, San Diego, CA, USA, 4–8 January 2016; AIAA 2016-0766. [CrossRef]
6. Langtry, R.B.; Kuntz, M.; Menter, F.R. Drag Prediction of Engine-Airframe Interference Effects with CFX-5. *J. Aircr.* **2005**, *42*, 1523–1529. [CrossRef]
7. Li, L.; Bai, J.; Qu, F. Multipoint Aerodynamic Shape Optimization of a Truss-Braced-Wing Aircraft. *J. Aircr.* **2022**, *59*, 1179–1194. [CrossRef]
8. Duggirala, R.K.; Roy, C.J.; Schetz, J.A. Analysis of Interference Drag for Strut-Strut Interaction in Transonic Flow. *AIAA J.* **2011**, *49*, 449–462. [CrossRef]
9. Maughmer, M.; Hallman, D.; Ruszkowski, R.; Chappel, G.; Waitz, I. Experimental investigation of wing/fuselage integration geometries. *J. Aircr.* **1989**, *26*, 705–711. [CrossRef]
10. Kegerise, M.A.; Neuhart, D.; Hannon, J.; Rumsey, C.L. An experimental investigation of a wing-fuselage junction model in the NASA Langley 14-by 22-foot subsonic wind tunnel. In Proceedings of the AIAA Scitech 2019 Forum, San Diego, CA, USA, 7–11 January 2019; Number 0077. [CrossRef]
11. Kubendran, L.; Bar-Sever, A.; Harvey, W. Flow control in a wing/fuselage-type juncture. In Proceedings of the 26th Aerospace Sciences Meeting, Reno, NV, USA, 11–14 January 1988; Number 614. [CrossRef]
12. Popelka, L.; Zeleny, L.; Simurda, D.; Matejka, M. Wing-Body Interaction: Numerical simulation, Wind-tunnel and In-flight Testing. *Tech. Soar.* **2010**, *34*, 29–36.
13. Adamidis, S.; Markatos, N. Mathematical Modelling and Comparative Numerical Simulations of wing-fuselage Junction Vortex Structures. *J. Aerosp. Eng. Mech.* **2022**, *6*, 555–587. [CrossRef]
14. Yildirim, A.; Mader, C.A.; Martins, J.R. A surface mesh deformation method near component intersections for high-fidelity design optimization. *Eng. Comput.* **2022**, *38*, 1393–1425. [CrossRef]
15. Hajdik, H.M.; Yildirim, A.; Martins, J.R. Aerodynamic shape optimization of filleted intersections with surface mesh deformation. In Proceedings of the ICAS 2024—34th Congress of the International Council of the Aeronautical Sciences, Florence, Italy, 9–13 September 2024; Number 227.
16. Biancolini, M.E.; Costa, E.; Cella, U.; Groth, C.; Veble, G.; Andrejašič, M. Glider fuselage-wing junction optimization using CFD and RBF mesh morphing. *Aircr. Eng. Aerosp. Technol.* **2016**, *88*, 740–752. [CrossRef]
17. Xu, S.; Timme, S.; Mykhaskiv, O.; Müller, J.D. Wing-body junction optimisation with CAD-based parametrisation including a moving intersection. *Aerosp. Sci. Technol.* **2017**, *68*, 543–551. [CrossRef]
18. Shang, J.S. Numerical simulation of wing-fuselage aerodynamic interaction. In Proceedings of the 21st Aerospace Sciences Meeting, Reno, NV, USA, 10–13 January 1983; Number 225. [CrossRef]
19. Milewski, W.M. Three-Dimensional Viscous Flow Computations Using the Integral Boundary Layer Equations Simultaneously Coupled with a Low Order Panel Method. Ph.D. Thesis, Massachusetts Institute of Technology, Cambridge, MA, USA, 1997.
20. Katz, J.; Plotkin, A. *Low-Speed Aerodynamics*, 2nd ed.; Cambridge Aerospace Series; Cambridge University Press: Cambridge, UK, 2001. [CrossRef]
21. MDOLab. Mach-Aero Framework. Available online: https://mdolab-mach-aero.readthedocs-hosted.com/en/latest/ (accessed on 1 February 2025).
22. Wu, E.; Kenway, G.; Mader, C.A.; Jasa, J.; Martins, J.R.R.A. pyOptSparse: A Python framework for large-scale constrained nonlinear optimization of sparse systems. *J. Open Source Softw.* **2020**, *5*, 2564. [CrossRef]
23. Mader, C.A.; Kenway, G.K.W.; Yildirim, A.; Martins, J.R.R.A. ADflow: An Open-Source Computational Fluid Dynamics Solver for Aerodynamic and Multidisciplinary Optimization. *J. Aerosp. Inf. Syst.* **2020**, *17*, 508–527. [CrossRef]
24. Kenway, G.K.W.; Mader, C.A.; He, P.; Martins, J.R.R.A. Effective Adjoint Approaches for Computational Fluid Dynamics. *Prog. Aerosp. Sci.* **2019**, *110*, 100542. [CrossRef]
25. Samareh, J.A. Survey of Shape Parameterization Techniques for High-Fidelity Multidisciplinary Shape Optimization. *AIAA J.* **2001**, *39*, 877–884. [CrossRef]
26. Zhang, T.; Wang, Z.; Huang, W.; Yan, L. A review of parametric approaches specific to aerodynamic design process. *Acta Astronaut.* **2018**, *145*, 319–331. [CrossRef]
27. Martins, J.R. Perspectives on aerodynamic design optimization. In Proceedings of the AIAA Scitech 2020 Forum, Orlando, FL, USA, 6–10 January 2020; Number 0043. [CrossRef]
28. Secco, N.R.; Kenway, G.K.W.; He, P.; Mader, C.; Martins, J.R.R.A. Efficient Mesh Generation and Deformation for Aerodynamic Shape Optimization. *AIAA J.* **2021**, *59*, 1151–1168. [CrossRef]

29. Zhao, H.; Kamensky, D.; Hwang, J.T.; Chen, J.S. Automated shape and thickness optimization for non-matching isogeometric shells using free-form deformation. In *Engineering with Computers*; Springer: Berlin/Heidelberg, Germany, 2024; pp. 1–24.
30. Brooks, T.R.; Kenway, G.K.; Martins, J.R. Benchmark aerostructural models for the study of transonic aircraft wings. *AIAA J.* **2018**, *56*, 2840–2855. [CrossRef]
31. Papoutsis-Kiachagias, E.; Giannakoglou, K.; Porziani, S.; Groth, C.; Biancolini, M.; Costa, E.; Andrejašič, M. Combining an OpenFOAM-based Adjoint Solver with RBF Morphing for Shape Optimization Problems on the RBF4AERO Platform. In *OpenFOAM®: Selected Papers of the 11th Workshop*; Springer: Berlin/Heidelberg, Germany, 2019; pp. 65–75.
32. Roache, P.J. *Verification and Validation in Computational Science and Engineering*; Hermosa Publisher: Tucson, AZ, USA, 1998; ISBN 978-0913478080.
33. Slater, J.W. Examining Spatial (Grid) Convergence. NASA. Available online: https://www.grc.nasa.gov/www/wind/valid/tutorial/spatconv.html (accessed on 1 February 2025).
34. Lyu, Z.; Xu, Z.; Martins, J.R. Benchmarking optimization algorithms for wing aerodynamic design optimization. In Proceedings of the 8th International Conference on Computational Fluid Dynamics, Chengdu, China, 14–18 July 2014; Number 0203.
35. Kenway, G.K.W.; Martins, J.R.R.A. Multipoint Aerodynamic Shape Optimization Investigations of the Common Research Model Wing. *AIAA J.* **2016**, *54*, 113–128. [CrossRef]